ACS APPLIED NANO MATERIALS

Open Access

This article is licensed under CC-BY 4.0

www.acsanm.org

Article

Synergistic Silver Doping and Halide Passivation for Enhanced Stability and Emission Efficiency in $CsPbI_3$ Quantum Dots

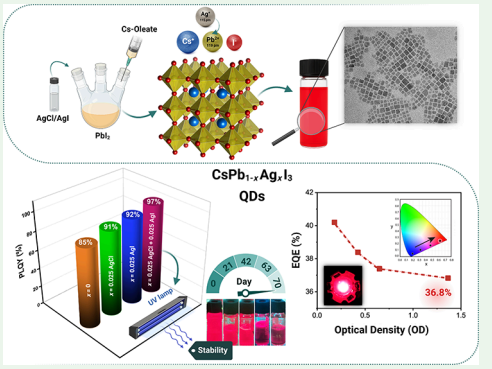
Pouriya Naziri, Asim Onal, Paul Simon, Saba Sepahban Shahgoli, Alp Yilmaz, Naeimeh Sadat Peighambardoust, Sedat Nizamoglu, and Umut Aydemir*

Cite This: *ACS Appl. Nano Mater.* 2025, 8, 20902−20914

Read Online

ACCESS | Metrics & More | Article Recommendations | Supporting Information

ABSTRACT: The intrinsic instability of $CsPbI_3$ quantum dots (QDs) presents a major challenge for their practical deployment in optoelectronic devices. Here, we demonstrate the combined effects of Ag^+ doping and halide (Cl^-/I^-) passivation to enhance the structural and optical stability of $CsPbI_3$ QDs. Partial substitution of Pb^{2+} by Ag^+ leads to lattice contraction and defect suppression, while Cl^- acts as a surface-localized passivating agent. Structural analyses (X-ray diffraction, high-resolution transmission electron microscopy, and high-resolution scanning transmission electron microscopy) confirm successful Ag^+ incorporation without secondary phase formation, and X-ray photoelectron spectroscopy depth profiling reveals surface enrichment of Cl^-. Mixed doping with AgCl and AgI precursors effectively stabilizes the cubic perovskite phase, increasing the photoluminescence quantum yield (PLQY) from ∼85 to 96.6% and reducing nonradiative recombination, as supported by time-resolved photoluminescence measurements. The optimized $CsPb_{1-x}Ag_xI_3$ (x = 0.025 AgCl + 0.025 AgI) exhibits outstanding photostability, retaining ∼41% of its initial PLQY after 70 days of continuous ultraviolet exposure. When integrated into red-emitting light-emitting diode devices, these QDs deliver external quantum efficiencies up to 36.8%, with stable and saturated emission. These results establish Ag^+/halide codoping as a powerful strategy to advance $CsPbI_3$ QDs toward robust and high-performance optoelectronic applications.



KEYWORDS: *perovskite quantum dots, silver doping, halide passivation, photoluminescence quantum yield, light-emitting diodes*

Downloaded via KOC UNIV on March 31, 2026 at 11:19:13 (UTC).
See https://pubs.acs.org/sharingguidelines for options on how to legitimately share published articles.

1. INTRODUCTION

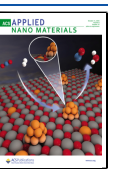
Metal halide perovskites (HPs) have attracted significant interest in optoelectronics due to their outstanding properties,[1] including high PLQY, long carrier diffusion lengths, low exciton binding energies, size-tunable emission, and low-cost synthesis.[2] These characteristics have enabled HPs to be widely used in LEDs,[2,3] solar cells,[4] photodetectors,[5] and even in emerging applications such as electrocatalysis[6] and photocatalysis.[7,8] Despite their promising optoelectronic performance, hybrid organic−inorganic perovskites ($APbI_3$) suffer from limited long-term stability, primarily due to the volatility of organic A-site cations, which accelerates degradation into PbI_2.[9] This limitation has motivated the development of fully inorganic $CsPbX_3$ (X = Cl, Br, or I) perovskites, which provide greater thermal and structural stability.[10] Among these, $CsPbI_3$ is particularly attractive owing to its optimal bandgap (∼1.73 eV) and excellent carrier dynamics.[11] However, its practical deployment is hindered by the instability of the desirable cubic α-phase at room temperature. The α-$CsPbI_3$ phase is only stable above 300 °C and readily transforms into the nonperovskite δ-phase under ambient conditions, severely impairing charge transport and emission characteristics.[9,12,13] This phase instability arises from structural distortion within the perovskite lattice, often described using the Goldschmidt tolerance factor (t):

$$t = \frac{r_A + r_X}{\sqrt{2}(r_B + r_X)}$$

where r_A, r_B, and r_X represent the ionic radii of the A-site cation (Cs^+), B-site cation (Pb^{2+}), and halide anion (I^-), respectively.[14] For $CsPbI_3$, t falls slightly below the ideal stability range ($0.8 \leq t \leq 1.0$), predisposing the material to lattice deformation and unwanted phase transitions.[15]

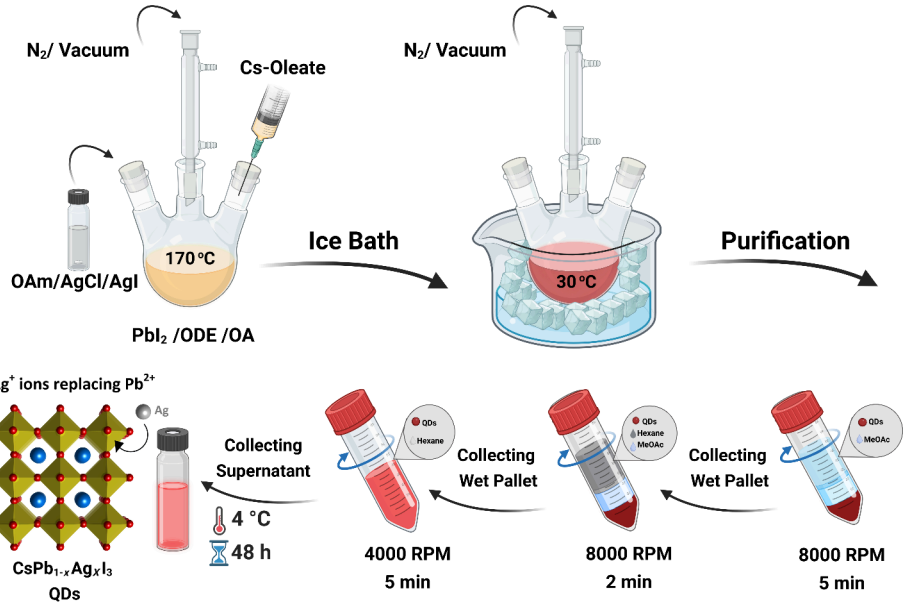
One widely adopted method to retain the α-phase at room temperature is the synthesis of $CsPbI_3$ in a QD form. Quantum confinement and high surface energy contribute to stabilizing the cubic phase in nanocrystals.[16] Nonetheless, $CsPbI_3$ QDs still suffer from halide deficiencies, particularly iodine vacancies

Received: August 8, 2025
Revised: September 24, 2025
Accepted: October 10, 2025
Published: October 20, 2025



© 2025 The Authors. Published by American Chemical Society

Scheme 1. Schematic Illustration of the Synthesis and Purification Process for Ag^+-Doped $CsPbI_3$ QDs ($CsPb_{1-x}Ag_xI_3$)



(V_I), which introduce trap states, accelerate nonradiative recombination, and compromise long-term photostability.[17] To address these issues, strategies such as compositional tuning,[18] surface modification,[19] ligand modification,[20] matrix encapsulation,[21] and cation/anion doping[22−24] have been explored. Among these, B-site doping, which involves the partial substitution of Pb^{2+} by aliovalent or isovalent cations, has proven especially effective in improving lattice stability, tailoring electronic structure, and mitigating defect states.[25,26] The incorporation of divalent (Mn^{2+},[27] Cu^{2+},[28] Co^{2+},[2] Zn^{2+},[17] Sr^{2+},[11,29] and Ni^{2+}[30]) and trivalent (Yb^{3+},[31] Ce^{3+},[32] La^{3+},[33] and In^{3+}[34]) dopants has been widely explored as a strategy to improve phase stability and suppress nonradiative recombination losses. By carefully selecting dopant ions with suitable ionic radii and chemical properties, it is possible to reinforce the perovskite lattice, effectively reducing lattice strain and mitigating the phase transition from the metastable α-phase to the undesirable δ-phase.[25,35]

In parallel, halide passivation strategies play a vital role in suppressing surface defects by introducing halide-rich environments or ionic additives. Halide anions such as Cl^-, Br^-, or I^- can bind to undercoordinated Pb^{2+} centers, reducing deep-level traps and nonradiative recombination.[17,36] Additionally, passivation helps prevent ion migration, smoothens surface roughness, and strengthens ligand binding at QD interfaces, key for improving device longevity.[37] Ligand engineering using organic surfactants or metal halide complexes further enhances colloidal stability and charge transport in QD-based devices.[38]

These advances have propelled perovskite QD LEDs (PQD-LEDs) toward high external quantum efficiencies (EQEs) across the visible spectrum.[2,39−41] However, due to their high surface-to-volume ratio, PQDs still exhibit a large density of surface traps and halide vacancies, limiting PLQY and device durability. To overcome this, combined strategies integrating cation doping with halide passivation have emerged as an effective route to synergistically enhance stability and efficiency.[11,42] By suppressing defect states and reinforcing lattice stability, these strategies substantially enhance optoelectronic performance, extend operational lifetimes (LTs), and facilitate the integration of $CsPbI_3$ QDs into next-generation displays, lighting systems, and LED technologies.[2,29,43,44]

In this study, we systematically investigated the effects of Ag^+ doping and halide passivation (Cl^- and I^-) on $CsPbI_3$ QDs to stabilize the α-phase and enhance optoelectronic performance. We employ AgCl, AgI, and a mixed doping strategy ($CsPb_{1-x}Ag_xI_3$ with x = 0.025 AgCl + 0.025 AgI) to simultaneously modulate lattice properties and passivate surface defects. Our findings reveal that the mixed-doped QDs achieve a remarkable PLQY of 96.63%, significantly higher than the undoped counterpart (85.14%), and exhibit superior photostability under continuous UV illumination for 70 days. Moreover, integration of these QDs into LED devices yields an impressive EQE of 36.8%, exceeding previously reported values for Pb-site-doped $CsPbI_3$ QDs. These results demonstrate that Ag^+ doping coupled with halide passivation offers a powerful pathway to realize stable and efficient perovskite QDs for next-generation optoelectronic applications.

2. EXPERIMENTAL SECTION

2.1. Materials. The following reagents were used in this study: lead(II) iodide (PbI_2, 99.999%, Sigma-Aldrich), cesium carbonate (Cs_2CO_3, 99%, Sigma-Aldrich), 1-octadecene (ODE, 90%, Sigma-Aldrich), oleylamine (OAm, 70%, Sigma-Aldrich), oleic acid (OA, 90%, Sigma-Aldrich), methyl acetate (MeOAc, ≥99.5%, Tekkim), silver chloride (AgCl, anhydrous, 99.7%, Alfa Aesar), silver iodide (AgI, 99.999%, Thermo Scientific), octane (98%, Sigma-Aldrich), and hexane (≥95%, Sigma-Aldrich). All chemicals were used as received without further purification.

2.2. Synthesis of the Cesium Oleate (Cs-Oleate) Precursor. The Cs-oleate precursor was synthesized following our previously reported procedure.[2] Briefly, 0.4 g of Cs_2CO_3 was mixed with 40 mL of ODE and 1.6 mL of OA in a three-neck flask and heated to 120 °C under vacuum for 30 min to eliminate residual moisture. The mixture was then purged with nitrogen gas for 10 min, and this degassing−purging cycle was repeated twice to ensure thorough removal of oxygen and water vapor. The resulting clear Cs-oleate solution was kept under a nitrogen atmosphere at 100 °C and used directly for subsequent synthesis steps.

2.3. Synthesis of Ag^+-Doped $CsPbI_3$ QDs. Ag^+-doped $CsPbI_3$ QDs ($CsPb_{1-x}Ag_xI_3$) were synthesized via a modified hot-injection

https://doi.org/10.1021/acsanm.5c03682
ACS Appl. Nano Mater. 2025, 8, 20902−20914

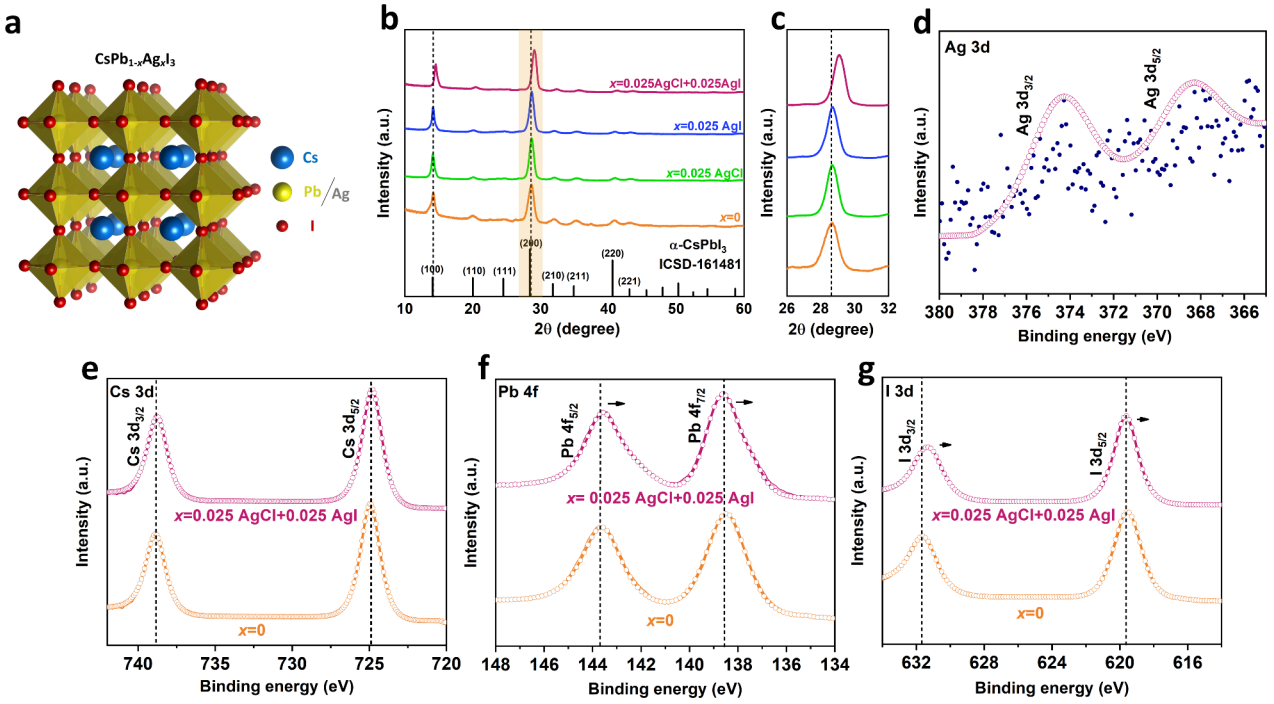


Figure 1. (a) Illustration of the $CsPb_{1-x}Ag_xI_3$ perovskite crystal structure. (b) XRD patterns of $CsPb_{1-x}Ag_xI_3$ QDs with different doping concentrations (x = 0, x = 0.025 AgCl, x = 0.025 AgI, and x = 0.025 AgCl + 0.025 AgI). (c) Magnified view of the (200) diffraction peaks, highlighting peak shifts due to Ag^+ incorporation. (d–g) High-resolution XPS spectra of undoped and $CsPb_{1-x}Ag_xI_3$ QDs (x = 0.025 AgCl + 0.025 AgI), displaying fitted core-level spectra for (d) Ag 3d, (e) Cs 3d, (f) Pb 4f, and (g) I 3d.

method based on our previous report.[2] Initially, 0.8 g of PbI_2 was dissolved in 40 mL of ODE and heated to 120 °C under vacuum for 1 h to remove residual moisture. The solution was then purged with nitrogen gas for 30 min. In parallel, AgCl and AgI dopants were separately predissolved in OAm at 70 °C under continuous stirring for 90 min. The dopant solutions, along with 4 mL each of OA and OAm, were added to the PbI_2 solution. The mixture was subjected to another 30 min vacuum treatment and a subsequent 10 min nitrogen purge to ensure complete degassing. The temperature was then raised to 170 °C, followed by the rapid injection of 6.4 mL of the preheated Cs-oleate precursor. After 5 s of reaction, the mixture was immediately quenched in an ice–water bath to terminate further QD growth. As the structural and optical characteristics of undoped $CsPbI_3$ QDs had been previously established,[2] these were used as reference standards without additional synthesis. The detailed procedure for precursor preparation, hot-injection synthesis, and subsequent purification is summarized in Scheme 1.

2.4. Purification of Ag^+-Doped $CsPbI_3$ QDs. The purification of $CsPb_{1-x}Ag_xI_3$ QDs was carried out using a standard precipitation–redispersion protocol. First, MeOAc was added to the crude QD solution at a 1:3 volume ratio (130 mL MeOAc), inducing precipitation. The mixture was centrifuged at 8000 rpm for 5 min, and the resulting pellet was redispersed in 9.6 mL of hexane. A second precipitation was performed by adding an equal volume of MeOAc, followed by centrifugation at 8000 rpm for 2 min. The QDs were then redispersed in 20 mL of hexane and centrifuged at 4000 rpm for 5 min to remove residual PbI_2 and Cs-oleate. The supernatant was stored in the dark at 4 °C for 48 h to allow further precipitation of excess Cs-oleate and Pb-oleate. After this aging period, the solution was gently decanted and subjected to a final centrifugation at 4000 rpm for 5 min. The resulting supernatant contained purified QDs, which were used for subsequent characterization and stability studies.

2.5. LED Fabrication. *2.5.1. Fabrication of Polydimethylsiloxane (PDMS) Lenses.* Hemispherical PDMS lenses were fabricated by mixing SYLGARD 184 elastomer with its curing agent in an 8:1 weight ratio. The mixture was thoroughly stirred, followed by vacuum degassing for 30 min to eliminate trapped air bubbles. The degassed PDMS was then cast into predesigned aluminum molds and cured at 100 °C for 40 min. Once fully solidified, the lenses were carefully extracted, yielding a hemispherical structure with an outer diameter of 9 mm and an inner cavity of 7 mm, optimized for efficient light dispersion.

2.5.2. LED Device Assembly. For LED integration, a blue LED chip was first securely mounted onto the circuit board as the excitation source. PDMS lenses were then placed over the LEDs and secured using NOA 68, a UV-curable polymer adhesive. To ensure durability and prevent leakage, the curing process was performed in two sequential steps: an initial 40 min UV exposure at 365 nm for preliminary bonding, followed by a second UV treatment to reinforce adhesion. This fabrication approach ensures optimal optical coupling and device stability, making the LED system suitable for performance characterization.

2.6. Characterizations. XRD measurements were performed using a Rigaku MiniFlex 600 X-ray diffractometer equipped with Cu Kα radiation (λ = 1.5418 Å). The diffraction patterns were captured over a 2θ range of 10–60° at a scanning rate of 1° per minute. XPS analysis was conducted using a Thermo Scientific K-Alpha XPS system, which utilized an Al Kα monochromator source (1486.6 eV). Spectral deconvolution was carried out with Avantage v5.99 software. For XRD and XPS measurements, QD samples were prepared by drop-casting a 0.5 mg/mL hexane solution onto silicon wafers, ensuring uniform film formation for analysis.

TEM images were acquired with a HITACHI HF5000 ColdFEG S/TEM instrument operating at 200 kV. Standard TEM analysis was performed using an FEI Tecnai F30-G2 microscope, equipped with a Super-Twin lens and a field emission gun operating at 300 kV. The microscope offers a point resolution of 2.0 Å and an information limit of approximately 1.2 Å. A wide-angle slow-scan CCD camera (MultiScan, 2k × 2k pixels; Gatan, Inc., USA) was used for image capture. The HR-TEM analyses of the samples were conducted using a double-corrected JEM-ARM300F electron microscope operating at 300 kV (Dresden Grand ARM, JEOL Company). The spherical aberration (Cs) of both the condenser and objective lens was corrected by dodecapole correctors in the beam (STEM) and in the

https://doi.org/10.1021/acsanm.5c03682
ACS Appl. Nano Mater. 2025, 8, 20902–20914

image (TEM) formation system. HR-TEM images were captured using a 4k × 4k pixel CCD array (Gatan US4000), providing a TEM resolution of 0.7 Å. All HR-TEM images presented in this article underwent Fourier filtering with a band-pass mask using Gatan Digital-Micrograph software. High-resolution scanning transmission electron microscopy (HR-STEM) images were captured using a high-angle annular dark-field (HAADF) detector with a semiangle of 64−180 mrad and a camera length of 10 cm. These images were recorded on a 4k × 4k pixel CCD array (Gatan US4000). The STEM resolution in dark-field mode is 0.5 Å.

PL, PLQY, and LT measurements were conducted using an Edinburgh Instruments FLS1000 fluorescence spectrometer equipped with an integrating sphere. QD samples were diluted in hexane to achieve an absorbance of 0.7 at 400 nm. PL and PLQY were measured using a xenon lamp with an excitation wavelength of 400 nm, while LT measurements were performed using a time-correlated single-photon counting (TCSPC) system coupled with a 377 nm pulsed laser (64 ps pulse width) and a pulse repetition period of 200 ns. In addition, all reported PLQY values represent averages of multiple independent measurements, with deviations within ±2%, further confirming the reliability of the data. UV−visible absorption spectra were recorded using a SHIMADZU UV-3600 spectrophotometer, and the bandgap energy of the QDs was determined from the absorbance data. Photostability testing was performed under controlled ambient conditions (temperature: 25−30 °C; relative humidity: 30−37%). QD dispersions were continuously irradiated with a 365 nm UVA lamp (Philips PL-S 9W/10/2P) to simulate prolonged operational conditions and assess environmental durability, particularly in the context of LED integration. The QD dispersions were stored in sealed glass vials to avoid solvent evaporation and external contamination and were continuously irradiated with the lamp positioned at a fixed distance of almost 25 cm from the samples. At this distance, the measured light intensity at the sample plane was approximately 1.2−1.5 mW cm^{-2}, which is consistent with conditions typically used for accelerated photostability testing of perovskite QDs.

3. RESULTS AND DISCUSSION

3.1. Structural Characterization. To investigate the structural impact of Ag^+ incorporation into $CsPbI_3$ QDs (Figure 1a), XRD measurements were carried out on both undoped and Ag^+-doped $CsPb_{1-x}Ag_xI_3$ (x = 0, 0.025, 0.05, 0.075, and 0.1) samples, using AgCl and AgI as separate dopant sources. To evaluate the combined effect of halide passivation, a mixed-dopant system (x = 0.025 AgCl + 0.025 AgI) was also prepared. The corresponding XRD patterns are shown in Figure 1b,c and Figure S1. All samples exhibit diffraction patterns characteristic of the cubic α-$CsPbI_3$ phase (ICSD-161481), with no detectable secondary phases or impurity peaks, confirming that Ag^+ ions are incorporated into the perovskite lattice without forming separate Ag-based compounds.

Close inspection of the (200) diffraction peaks reveals subtle yet important concentration-dependent effects specific to each dopant source. For AgCl doping (Figure S1a), most samples (x = 0, 0.025, 0.075, and 0.1) exhibit nearly identical (200) peak positions. However, at x = 0.05, a distinct shift toward higher 2θ angles occurs, clearly indicating lattice contraction. This contraction mainly results from substitution of Pb^{2+} by smaller Ag^+ ions (ionic radius = 115 pm vs Pb^{2+} = 119 pm). Although Cl^- ions (181 pm) primarily passivate surface defects, their incorporation into bulk lattice sites is likely minimal, thus not significantly contributing to the observed lattice contraction.[2,45,46] The absence of further peak shifts at higher doping levels (x = 0.075 and 0.1) implies a saturation threshold, beyond which excess AgCl may remain primarily at the QD surface or form localized clusters, rather than further incorporating into the lattice.

In contrast, AgI-doped samples (Figure S1b) display almost no change in the (200) diffraction peak position for doping concentrations up to x = 0.075, indicating limited lattice distortion and minimal incorporation of Ag^+ ions at these levels. Notably, only at the highest doping concentration (x = 0.1) does the peak position shift toward lower 2θ angles, suggesting lattice expansion. This expansion likely arises from structural defects, strain, or surface-segregated Ag-rich species, formed once the lattice solubility limit of Ag^+ is exceeded. Additionally, the mixed-dopant sample (x = 0.025 AgCl + 0.025 AgI, Figure 1b,c) shows a clear shift toward higher angles, similar to the x = 0.05 AgCl-doped sample. The observed trends suggest that at optimal concentrations ($x \leq$ 0.05), Ag^+ doping can effectively enhance lattice stability and phase retention by increasing the Goldschmidt tolerance factor. However, at higher doping levels, defect-induced distortions and strain effects become more significant and may introduce additional stress on the crystal structure, affecting long-term stability and optoelectronic performance. It should be noted that XRD may not be sufficiently sensitive to detect small compositional changes or low levels of dopant inclusion, especially in nanocrystalline samples, and complementary techniques such as XPS or HR-STEM are often needed to confirm incorporation at low doping concentrations.

To further probe the chemical environment of the dopants, XPS analysis was performed on the mixed-dopant $CsPb_{1-x}Ag_xI_3$ QDs (x = 0.025 AgCl + 0.025 AgI) and compared to undoped $CsPbI_3$. The survey spectrum (Figure S2) confirms the presence of Cs, Pb, I, and Ag without any unexpected impurities, reinforcing the phase purity observed by XRD. High-resolution XPS spectra of the Ag 3d region (Figure 1d) reveal peaks at 368.2 and 374.2 eV, corresponding to Ag $3d_{5/2}$ and Ag $3d_{3/2}$, respectively, which is typical of Ag^+ in an ionic environment. The absence of metallic Ag peaks indicates that Ag^+ is incorporated into the lattice rather than forming Ag^+ inclusions.[47] The Cs 3d peaks (Figure 1e) remain nearly unchanged after doping, indicating that Cs^+ ions at the A-site are unaffected by Ag^+ incorporation. However, a distinct shift is observed in the Pb 4f region (Figure 1f), where the Pb $4f_{7/2}$ and $4f_{5/2}$ peaks shift from 138.2 and 143.4 eV in the undoped sample to 137.8 and 142.6 eV, respectively, in the doped sample. This shift reflects changes in the local chemical environment and partial replacement of Pb^{2+} by Ag^+.

In perovskite QDs, Pb^{2+} typically exists in two coordination environments: Pb−I in the crystal lattice and Pb−oleate on the surface.[48] Peak deconvolution (see Figure S3) supports this distinction. The observed downshift in binding energy suggests reduced Pb−I bond strength and local charge redistribution induced by Ag^+ substitution.[46] A similar trend is evident in the I 3d spectra (Figure 1g), where I $3d_{5/2}$ and I $3d_{3/2}$ peaks shift by ∼0.23 eV toward lower binding energy upon doping. This shift is attributed to stronger Ag−I bonding interactions and a reduced density of iodine vacancies. Given Ag^+'s higher electronegativity (1.93) relative to Pb^{2+} (2.33), the observed spectral changes likely stem from altered charge-transfer dynamics and lattice polarization.

Figure S4 presents the Cl 2p XPS spectra of $CsPb_{1-x}Ag_xI_3$ (x = 0.025 AgCl + 0.025 AgI) QDs, measured both at the surface and after 360 s of Ar ion etching. The two distinct peaks corresponding to Cl $2p_{1/2}$ and Cl $2p_{3/2}$ are clearly visible at the surface, confirming the presence of residual Cl^- ions in the

https://doi.org/10.1021/acsanm.5c03682
ACS Appl. Nano Mater. 2025, 8, 20902−20914

QDs. Upon ion etching, the intensity of these peaks significantly diminishes, indicating that Cl^- ions are predominantly confined to the surface region rather than incorporated into the perovskite lattice.

This surface-localized distribution of Cl^- supports its function as a passivating agent, most likely filling iodine vacancies and mitigating halide-related surface defects. Such effective passivation leads to a reduction in trap-state density, thereby improving colloidal stability and suppressing nonradiative recombination pathways. Consequently, the remarkably low defect density observed in $CsPb_{0.95}Ag_{0.05}I_3$ QDs can be attributed not only to Ag^+ doping within the lattice but also to the synergistic surface passivation provided by Cl^- ions derived from AgCl. This combined doping−passivation strategy is crucial in enhancing the structural integrity and optoelectronic performance of the QDs, as further evidenced by their superior optical stability and PLQY.

Together, the XRD and XPS results confirm that Ag^+ ions substitute Pb^{2+} at the B-site of the perovskite lattice, leading to structural contraction, chemical state modification, and defect passivation. These effects are most pronounced at moderate doping levels ($x \leq 0.05$), beyond which Ag^+ incorporation becomes energetically or structurally unfavorable. The observed binding energy shifts further suggest that Ag^+ incorporation modulates the electronic structure, which could have implications for the optical and stability properties of $CsPb_{1-x}Ag_xI_3$ QDs.

3.2. Morphological Study. Low-magnification TEM images of $CsPb_{1-x}Ag_xI_3$ QDs (x = 0.025 AgCl + 0.025 AgI) are shown in Figures 2a,b, revealing a densely packed assembly of nanocrystals ranging from 4 to 18 nm in size. Larger particles (>10 nm) predominantly exhibit cubic or rectangular morphologies with well-defined, faceted edges, indicative of high crystallinity. In contrast, smaller QDs (<10 nm) tend to display truncated geometries, likely resulting from surface energy minimization and anisotropic growth during nucleation. These QDs self-assemble into well-ordered superstructures with an average periodicity of ∼15 nm × 15 nm, indicating excellent size uniformity. Within a 250 nm × 250 nm scan area, only minor orientational deviations (±15°) are observed, suggesting slight misalignments during self-organization. The coexistence of cubic and truncated forms points to possible stabilization of multiple crystallographic facets, potentially facilitated by Ag^+ incorporation and halide (Cl^-/I^-) surface passivation.

High-resolution TEM (HR-TEM) images of (Figure 2c−h and Figure S5a−d) provide atomic-scale insights into the morphology and defect landscape of $CsPb_{0.95}Ag_{0.05}I_3$ QDs, viewed along the [100] zone axis. In Figure 2c,d, a truncated octahedral QD (∼8 nm × 6 nm) shows atomically sharp terminations and a highly ordered internal lattice. Bragg filtering (Figure 2d) reveals periodic atomic columns, with the highest contrast corresponding to heavier Pb atoms. The regularity of the lattice confirms successful Ag^+ substitution at Pb^{2+} sites without significant structural disruption. Figure 2e,f presents a larger QD (∼13 nm × 8 nm) with a distinctly elongated aspect ratio. The high-resolution image (Figure 2e) reveals a well-defined crystal structure, while the Bragg-filtered counterpart (Figure 2f) exposes localized lattice distortions. Specifically, the red oval highlights regions where atomic columns appear disordered or smeared along the *c*-direction, indicating a loss of lattice coherence. This disruption is attributed to the presence of interstitial defects, where excess

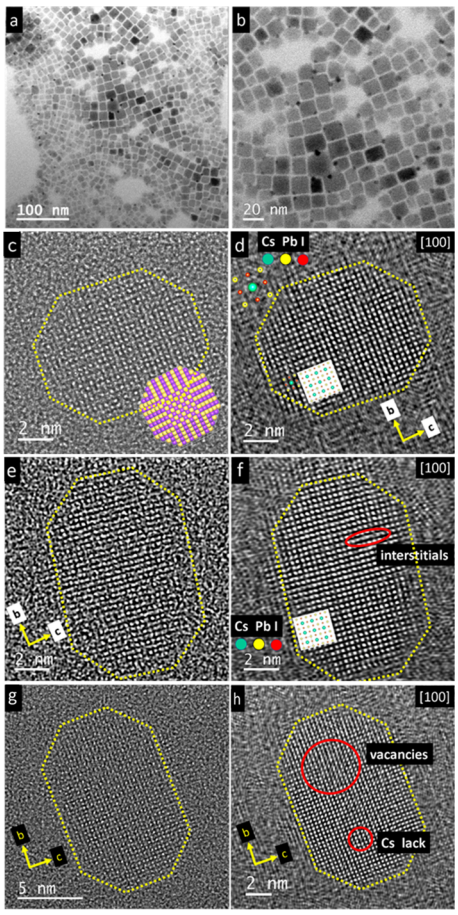


Figure 2. (a, b) Low-magnification TEM images of $CsPb_{0.95}Ag_{0.05}I_3$ QDs, showing a densely packed assembly of cubic-shaped and tetragonal nanocrystals. The QDs form a highly ordered superstructure with ∼15 nm × 15 nm periodicity and an orientational deviation of ±15° across a 250 nm × 250 nm area. (c) HR-TEM image and (d) corresponding Bragg-filtered image of a truncated octahedral QD (∼8 nm × 6 nm) with an elongated morphology, viewed along the [100] zone axis. The atomic columns are well-resolved, indicating high crystallinity. (e, f) HR-TEM image and Bragg-filtered image of a larger QD (∼13 nm × 8 nm), displaying delocalized and smeared atomic contrast along the *c*-direction. The red oval in (f) highlights regions of diminished lattice coherence caused by interstitial defects, likely involving excess Cs or I atoms occupying nonlattice sites. (g, h) HR-TEM image and Bragg-filtered image of a QD (∼13 nm × 9 nm) viewed along the [001] zone axis. A ∼1 nm disordered region at the upper right (red circle) is attributed to lattice vacancies, while a single Cs^+ vacancy at the lower edge is marked by a smaller red circle.

atoms, likely Cs or I, occupy nonideal lattice positions, distorting the periodicity. These interstitials may result from local strain accumulation, surface relaxation, or uneven dopant distribution during crystal growth. The observed anisotropic disorder, aligned with the elongation axis, suggests that kinetic factors during synthesis such as facet-specific growth rates or dopant segregation could influence defect formation and spatial distribution. Figure 2g,h shows another QD (∼13 nm × 9 nm) along the [100] direction, exhibiting visible point defects. A ∼1 nm-wide region at the top displays disrupted atomic contrast, likely due to lattice vacancies or local strain accumulation (red circle). A single Cs^+ vacancy is also identifiable at the bottom edge (small red circle), suggesting A-site instability or incomplete occupancy. These point defects,

https://doi.org/10.1021/acsanm.5c03682
ACS Appl. Nano Mater. 2025, 8, 20902−20914

particularly at the QD surface, could serve dual roles, either as nonradiative recombination centers or as sites for defect passivation via ligand or dopant coordination. Additional HR-TEM images in Figure S5a–d reinforce the prevalence of truncated octahedral morphologies (~10 nm), exhibiting uniform lattice fringes with minimal disorder. These observations support the notion that mixed Ag^+ doping (x = 0.025 AgCl + 0.025 AgI) contributes to enhanced structural stability by mitigating lattice strain and suppressing defect formation.

Overall, the presence of both truncated and elongated QD morphologies reflects a balance between thermodynamically favored shapes and kinetically controlled growth. The occurrence of point defects (vacancies and interstitials) and lattice disorder in larger QDs aligns with XPS-derived evidence of local charge redistribution and is consistent with the observed reduction in PL lifetimes, both of which are indicative of partial Ag^+ incorporation and evolving electronic structure.

High-angle annular dark-field scanning transmission electron microscopy (HAADF-STEM) imaging, which emphasizes heavier elements such as Pb through Z-contrast sensitivity, was employed to investigate the structural characteristics of $CsPb_{0.95}Ag_{0.05}I_3$ QDs (Figure 3a–d and Figure S6a–d). The 3D surface plot in Figure 3a reveals a densely packed array of QDs with a narrow interparticle spacing and uniform spatial distribution. The presence of cubic and truncated octahedral morphologies confirms controlled synthesis and low polydispersity. The high central intensity observed in individual dots predominantly arises from Pb atomic columns due to their significantly higher atomic number and resulting stronger scattering contrast in HAADF-STEM. While Cs and I are also relatively heavy elements, their contribution to the image contrast is comparatively lower, making Pb the primary contributor to the observed intensity. The uniformity and brightness of these features indicate excellent crystallinity and phase purity. A representative high-resolution image of a single nanoparticle (~13 nm × 9 nm), shown in Figure 3b–d, demonstrates well-resolved atomic columns and sharp lattice periodicity. The fast Fourier transform (FFT) pattern (Figure 3d) confirms the cubic crystal symmetry along the [001] zone axis, with indexed diffraction spots corresponding to the (100) and (010) planes.

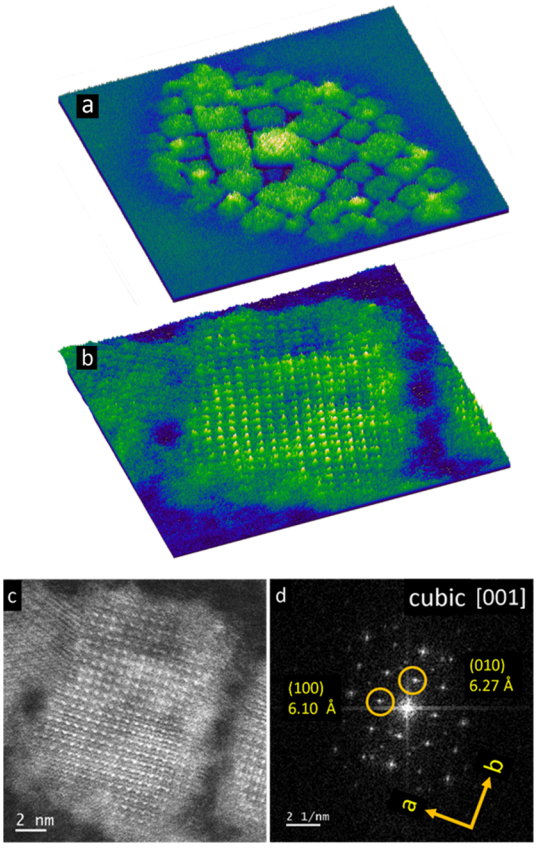


Figure 3. HR-STEM images of $CsPb_{0.95}Ag_{0.05}I_3$ cubic QDs in the [001] orientation. Mostly heavy lead is registered at the high-angle annular dark-field mode in STEM. (a) 3D overview scan image of the QD assembly. (b–d) STEM images with FFT analysis of selected nanoparticles showing the [001] orientation of the cubic phase. The particle size amounts to 13 nm × 9 nm.

The retention of cubic symmetry at this particle size underscores the structural robustness of $CsPbI_3$ QDs upon optimized Ag^+ doping, effectively suppressing the transition to the nonperovskite orthorhombic phase, a key challenge for stability in all-inorganic perovskites. Figure S6a,b displays a smaller QD (~6 nm in diameter), which still exhibits sharp lattice fringes and a clean, defect-free surface. These observations indicate that Ag^+ doping not only stabilizes the larger QDs but also preserves crystallinity and surface order in smaller nanocrystals, which is an essential factor for optoelectronic applications where quantum confinement effects become significant. Figure S6c,d presents an ultrasmall QD (~5 nm, approximately eight unit cells in width). Despite its size, the QD maintains a cubic lattice with well-aligned planes and no apparent distortions, further validating the effectiveness of codoping at an optimal concentration (x = 0.025 AgCl + 0.025 AgI) in stabilizing the perovskite phase and suppressing surface disorder. Unlike undoped $CsPbI_3$ QDs, which often exhibit significant lattice distortions at this scale, these Ag-doped QDs retain structural integrity even near the quantum confinement limit.

To confirm the elemental composition and successful incorporation of Ag^+ into the perovskite lattice, energy-dispersive X-ray spectroscopy (EDS) analysis was conducted on $CsPb_{0.95}Ag_{0.05}I_3$ QDs. The resulting EDS spectrum (Figure S7) clearly shows characteristic peaks corresponding to Cs, Pb, I, Ag, and Cl, confirming the presence of all intended constituents. Quantitative analysis (Table S1) reveals atomic percentages of approximately 34.78% Pb, 8.46% Cs, 50.57% I, and 3.26% Cl. While these values deviate from the exact 1:1:3 stoichiometry of $CsPbI_3$, such deviations are common in EDS measurements due to its surface-sensitive nature and sample-to-sample variability at the nanoscale. Nevertheless, the relative elemental ratios remain broadly consistent with the targeted perovskite composition, supporting the successful formation of $CsPb_{1-x}Ag_xI_3$ QDs. The measured Ag content is approximately 2.93 at. %, slightly below the nominal 5 mol. % relative to Pb^{2+}. During the synthesis of doped QDs, achieving a perfectly uniform distribution of dopants like Ag^+ can be challenging. Localized areas might have higher or lower concentrations, leading to variations in the measured content depending on the region analyzed. Such variation aligns with previous studies.[49,50]

TEM was used to investigate the morphological evolution of $CsPb_{1-x}Ag_xI_3$ QDs with varying Ag^+ concentrations. As shown in Figure 4 and Figures S8 and S9, all samples exhibit well-

https://doi.org/10.1021/acsanm.5c03682
ACS Appl. Nano Mater. 2025, 8, 20902–20914

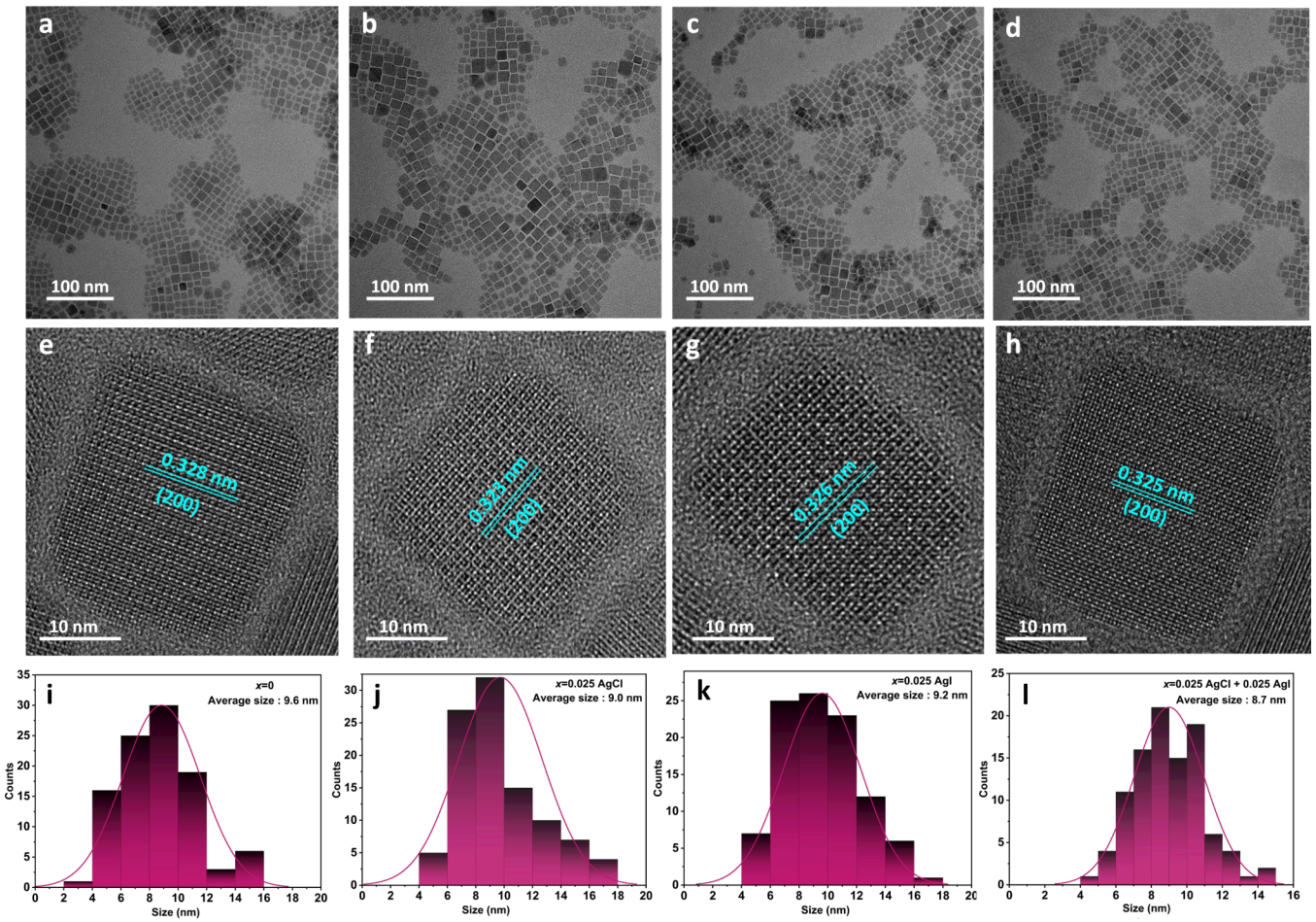


Figure 4. (a–d) TEM images, (e–h) HR-TEM images, and (i–l) size distribution histograms of $CsPb_{1-x}Ag_xI_3$ QDs with different doping concentrations: (a, e, and i) $x = 0$ (undoped $CsPbI_3$), (b, f, and j) $x = 0.025$ (AgCl), and (c, g, and k) $x = 0.025$ (AgI), and (d, h, l) $x = 0.025$ AgCl + 0.025 AgI.

faceted cubic or truncated shapes with narrow size distributions, indicating that Ag^+ doping does not compromise the overall morphological integrity of the QDs. The average particle size progressively decreases with Ag^+ incorporation. Undoped $CsPbI_3$ QDs exhibit a mean diameter of 9.6 nm, whereas doping with AgCl ($x = 0.025$), AgI ($x = 0.025$), and the combined AgCl + AgI system ($x = 0.05$ total) yields smaller sizes of 9.0, 9.2, and 8.7 nm, respectively (Figure 4i–l). Notably, the mixed-dopant system produces the most uniform and size-homogeneous QDs, suggesting a synergistic effect of the two halide sources in modulating crystal growth. This reduction in size is attributed to the presence of excess halide ions during synthesis, which modulate nucleation and crystal growth kinetics by passivating the QD surface and limiting lattice expansion.[2,37]

HR-TEM images (Figure 4e–h) further demonstrate that Ag^+ doping induces a gradual decrease in the interplanar spacing of the (200) lattice planes: from 0.328 nm (undoped) to 0.323 nm (AgCl-doped), 0.326 nm (AgI-doped), and 0.325 nm (AgCl + AgI-doped). This trend reflects lattice contraction due to the substitution of Pb^{2+} (ionic radius = 119 pm) by the smaller Ag^+ ions (115 pm), resulting in shortened bond lengths and a more compact perovskite structure.[51] These results are in excellent agreement with XRD peak shifts to higher angles, further validating the structural impact of Ag^+ incorporation. Further analysis in Figure S8 (AgCl-doped QDs) confirms that both the particle size and *d*-spacing decrease with increasing Ag^+ concentration up to $x = 0.05$. However, at higher doping levels ($x = 0.075$ and 0.1), an inverse trend is observed: the particle size and *d*-spacing begin to increase. This suggests a saturation threshold for Ag^+ substitution, beyond which excess silver is no longer efficiently incorporated into the lattice and may instead form surface defects or minor secondary phases. Similarly, Figure S9 (AgI-doped QDs) shows a decrease in QD size and *d*-spacing up to $x = 0.05$. Beyond this level, at $x = 0.075$ and 0.1, the QD size increases unexpectedly. This behavior is likely due to phase segregation or Ag^+ accumulation at the QD surface or in near-surface regions, once the solubility limit is exceeded. Such accumulation can alter surface energy and facilitate the growth of larger crystallites. These observations align with structural and optical characterizations, further supporting the hypothesis of doping-induced surface modifications and local compositional heterogeneity at elevated Ag^+ concentrations.

Taken together, these results suggest that Ag^+ plays a dual role in QD formation: (i) it induces lattice contraction through partial substitution of Pb^{2+}, thereby enhancing structural stability, and (ii) it modulates particle size via halide-assisted control over nucleation and growth kinetics. While moderate doping ($x \leq 0.05$) leads to smaller, more uniform QDs with well-defined crystallinity, excessive Ag^+ loading ($x > 0.05$) results in competing effects, crystallite enlargement, deviation

https://doi.org/10.1021/acsanm.5c03682
ACS Appl. Nano Mater. 2025, 8, 20902–20914

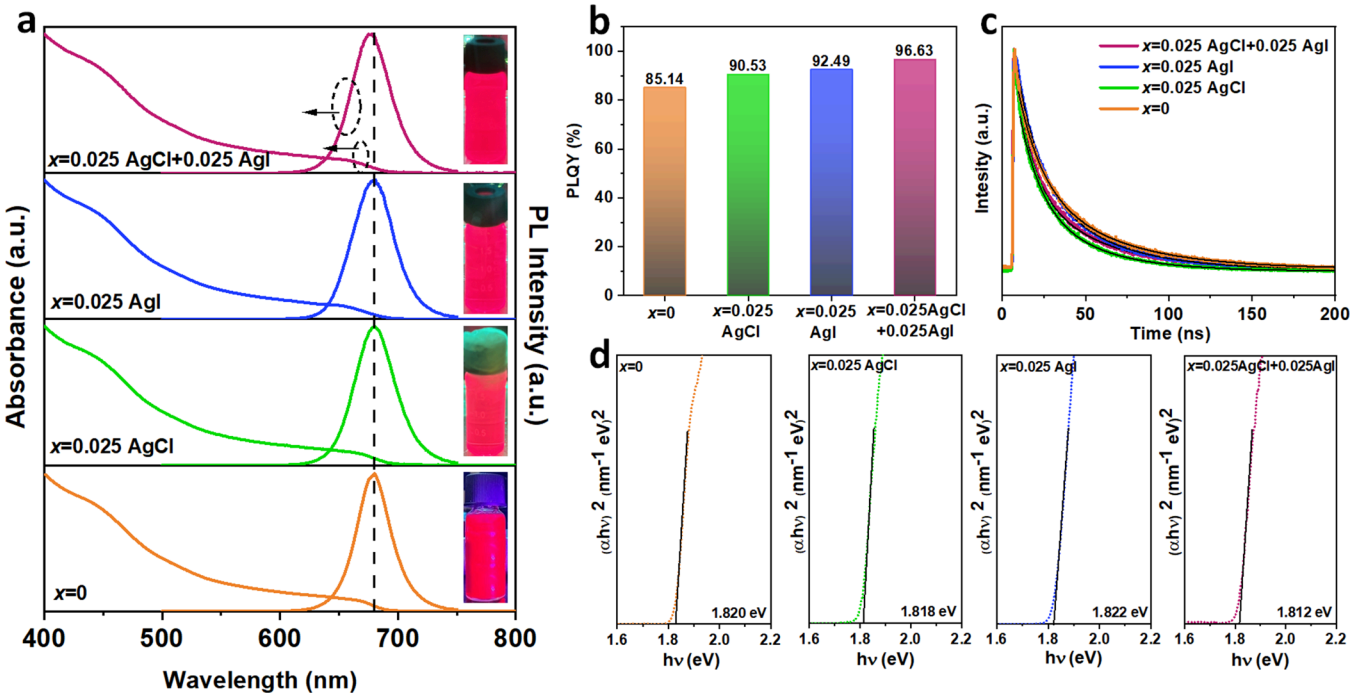


Figure 5. (a) Normalized absorption and PL spectra of $CsPb_{1-x}Ag_xI_3$ QDs (the right insets show the corresponding colloidal solutions illuminated under UV light), (b) corresponding PLQYs as a function of Ag^+ doping concentration (x), (c) TRPL decay curves of $CsPb_{1-x}Ag_xI_3$ QDs (x = 0, 0.025 AgCl, 0.025 AgI, and 0.025 AgCl + 0.025 AgI), and (d) Tauc plots extracted from absorption spectra, illustrating the estimated bandgap values for undoped and Ag^+-doped QDs.

from ideal stoichiometry, and potential surface or phase inhomogeneities. In parallel, the Cl^- and I^- anions introduced via AgCl and AgI precursors act as surface passivating agents, minimizing vacancy-type defects and suppressing surface-related disorder, as confirmed by HR-TEM and XPS depth profiling. The combined insights from EDS, TEM, HR-TEM, and XRD provide a coherent picture of how Ag^+ doping and halide passivation together influence the morphology, lattice characteristics, and growth dynamics of $CsPbI_3$ QDs. These structural modifications are closely linked to the enhanced optical properties and long-term stability discussed in subsequent sections.

3.3. Optical Characterization. To evaluate the impact of Ag^+ incorporation on the optical properties of $CsPbI_3$ QDs, we systematically investigated the absorption, PL, PLQY, and time-resolved PL (TRPL) characteristics of undoped and Ag^+-doped $CsPb_{1-x}Ag_xI_3$ QDs. Doping was performed using AgCl and AgI sources at various concentrations (x = 0.025, 0.05, 0.075, and 0.1), as well as a mixed-dopant sample (x = 0.025 AgCl + 0.025 AgI). The results are summarized in Figure 5 and Figures S10–S12.

As shown in Figure 5a, the optical absorption and PL spectra of $CsPb_{1-x}Ag_xI_3$ QDs exhibit a doping-dependent blueshift. At low doping (x = 0.025 AgCl), the excitonic absorption (667 nm) and PL peaks (680 nm) remain essentially unchanged compared to the undoped QDs, suggesting that limited Ag^+ substitution does not significantly alter the electronic structure. In contrast, a slight blueshift in the absorption peak is observed for x = 0.025 AgI (to 664 nm), while the PL emission remains fixed at 680 nm. Notably, codoping with AgCl and AgI (x = 0.025 + 0.025) leads to a more pronounced shift in both spectra, with absorption and PL peaks at 665 and 677 nm, respectively, indicating a greater influence of mixed doping on the band structure. At higher AgCl concentrations (x = 0.05 and 0.075), both the absorption and PL peaks continue to blueshift, reaching 663 and 675 nm, respectively, consistent with increased lattice contraction. However, this trend reverses at x = 0.1, where further blueshifting is not observed. A similar nonmonotonic trend is evident for AgI-doped QDs: blueshifts persist up to x = 0.05, while higher doping levels (x = 0.075 and 0.1) result in a redshift of the PL peak to 682 and 684 nm and absorption edges returning toward their original positions. These deviations at high doping levels suggest a saturation threshold for effective Ag^+ incorporation. Beyond this point, excess Ag^+ may induce lattice strain, form surface-bound species, or introduce nonuniform doping, leading to band-edge disorder or exciton localization. This interpretation aligns with structural characterizations (XRD and TEM), which indicate limited lattice incorporation and increased defect formation at elevated Ag concentrations.

The fwhm of PL peaks provides additional insight into the structural and electronic uniformity. For AgCl-doped QDs (Figure S10b), fwhm initially increases from 37.27 nm (undoped) to 42.25 nm at x = 0.025, likely due to slight size distribution broadening. At higher doping levels, the fwhm decreases, reflecting a partial recovery of emission homogeneity. Similar trends are observed in AgI-doped QDs (Figure S11b), with fwhm peaking at 42.91 nm (x = 0.025) and declining to 36.86 nm at x = 0.1. PLQY values shown in Figure 5b support these trends. Ag^+ doping significantly enhances emission efficiency at lower concentrations, increasing PLQY from 85.14% (undoped) to 90.53% (x = 0.025 AgCl) and 92.49% (x = 0.025 AgI) and peaking at 96.63% for the mixed-dopant QDs. This improvement is attributed to effective passivation of trap states and reduced nonradiative recombination. The mixed system demonstrates a synergistic effect, where Ag^+ incorporation and halide copassivation cooperate to yield near-unity PLQY. This aligns well with our previous

https://doi.org/10.1021/acsanm.5c03682
ACS Appl. Nano Mater. 2025, 8, 20902−20914

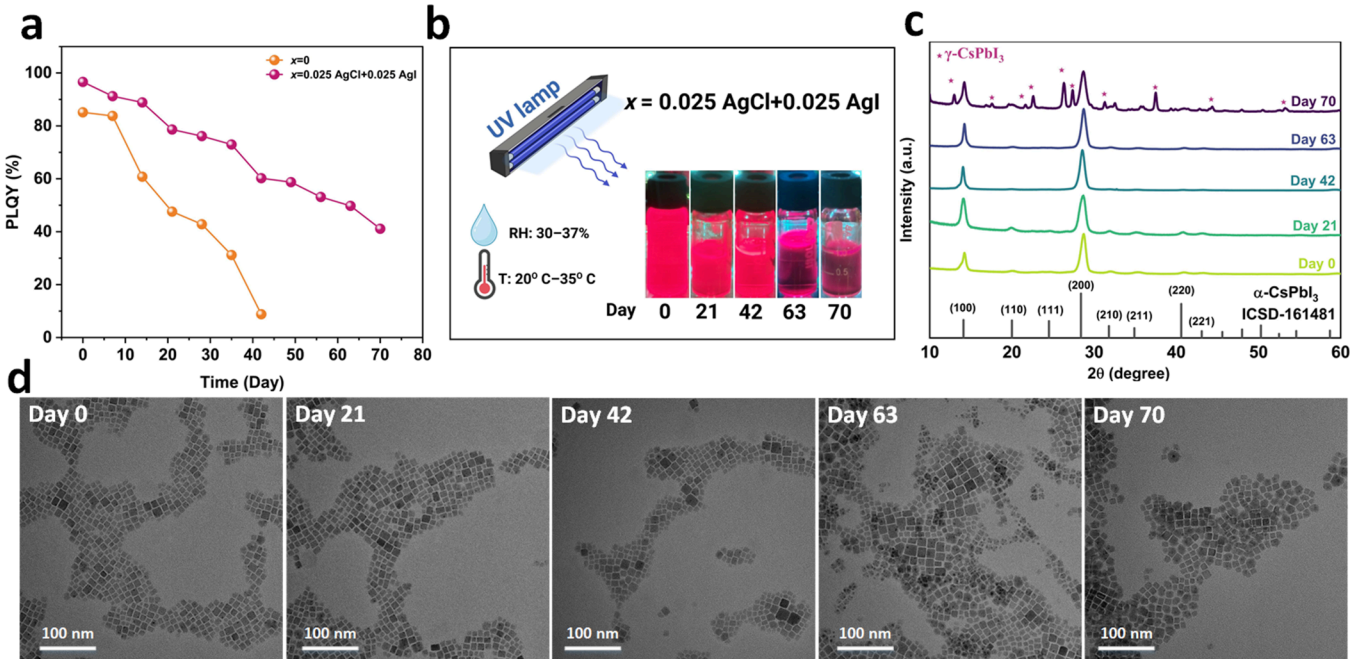


Figure 6. Stability evaluation of $CsPb_{1-x}Ag_xI_3$ QDs under continuous UV exposure. (a) PLQY decay over time for undoped and x = 0.025 AgCl + 0.025 AgI-doped $CsPbI_3$ QDs, demonstrating enhanced photostability of the mixed-doped sample; (b) digital images of colloidal QD solutions under UV light illumination at different aging intervals (day 0, 21, 42, 63, and 70); and (c, d) XRD patterns and TEM images of the $CsPb_{1-x}Ag_xI_3$ (x = 0.025 AgCl + 0.025 AgI) QDs over time.

study on perovskite QDs, where dual-passivation strategies lead to superior optoelectronic performance.[2] At higher doping levels, however, PLQY declines sharply, falling to 63.86% (x = 0.1 AgCl) and 74.53% (x = 0.1 AgI) (Figures S10b and S11b), indicating that excessive Ag^+ incorporation introduces new defect states that act as nonradiative recombination centers, ultimately reducing emission efficiency.

To further understand the recombination dynamics, TRPL measurements were conducted (Figure 5c and Figure S12a,b), and decay curves were fitted using a biexponential model (see Table S2). Two lifetimes were extracted: τ_1 (short component, nonradiative) and τ_2 (long component, radiative).[52] The average PL lifetime (τ_{av}) decreases upon moderate Ag^+ doping, from 46.93 ns (undoped) to 34.59 ns (x = 0.025 AgCl), 38.28 ns (x = 0.025 AgI), and 39.44 ns. This decrease in τ_{av} suggests that Ag^+ doping effectively modifies charge carrier dynamics, likely by mitigating iodine vacancy (V_I) defects, which are known to introduce shallow trap states that prolong carrier lifetimes. At higher doping levels (x > 0.05), a further shortening of τ_{av} is observed, but this is attributed to increased nonradiative decay, indicating a shift from beneficial defect passivation to defect formation. These results reinforce the conclusion that controlled Ag^+ incorporation ($x \leq 0.05$) optimizes recombination dynamics, while overdoping introduces structural disruptions.

Bandgap evolution, extracted from Tauc plots (Figure 5d), shows only minor changes across doping concentrations. The direct bandgap slightly narrows from 1.820 eV (undoped) to 1.812 eV in the mixed-dopant sample. This minimal change suggests that the primary effect of Ag^+ doping is on defect passivation rather than direct bandgap modulation. A possible explanation for this could be the compensating effects of Ag^+ substitution and lattice contraction, which counteract bandgap widening that typically occurs with smaller ionic dopants.

3.4. Stability Tests. To assess the photostability of $CsPb_{1-x}Ag_xI_3$ QDs under continuous UV exposure, mixed-doped QDs (x = 0.025 AgCl + 0.025 AgI) were compared to undoped $CsPbI_3$, based on their superior initial PLQY. All samples were stored under ambient conditions (20−35 °C, RH: 30−37%) and irradiated with 365 nm UV light for 70 days.

As shown in Figure 6a, the undoped $CsPbI_3$ QDs experienced rapid degradation, with PLQY dropping from 85.14 to 8.82% by day 42. This decline reflects the known instability of $CsPbI_3$ under illumination, primarily due to defect-assisted nonradiative recombination and phase degradation under prolonged illumination.[2]

In stark contrast, the mixed-doped QDs exhibited markedly enhanced stability, retaining 78.62% of their initial PLQY after 21 days, 60.23% after 42 days, and 41.12% even after 70 days of UV exposure. The gradual decline suggests a significant suppression of degradation mechanisms. Figure 6b further confirms these results through UV-excited images, which show sustained red luminescence in the mixed-doped samples over time.

This enhanced photostability of $CsPb_{1-x}Ag_xI_3$ QDs with mixed AgCl and AgI is attributed to a synergistic defect passivation mechanism. Ag^+ ions substitute Pb^{2+} at B-sites, reducing undercoordinated Pb sites and suppressing trap states, while halide codoping with Cl^- and I^- fills halide vacancies and reinforces the perovskite lattice. Cl^- incorporation leads to slight lattice contraction and a higher Goldschmidt tolerance factor, stabilizing the cubic phase, while I^- enhances charge transport and prevents charge accumulation, together maintaining both optical and structural integrity. TEM analysis (Figure 6d) supports these findings. The mixed-doped QDs retained their well-defined cubic morphology and narrow size distribution throughout the 70-day test period. Only slight edge rounding was observed in

https://doi.org/10.1021/acsanm.5c03682
ACS Appl. Nano Mater. 2025, 8, 20902−20914

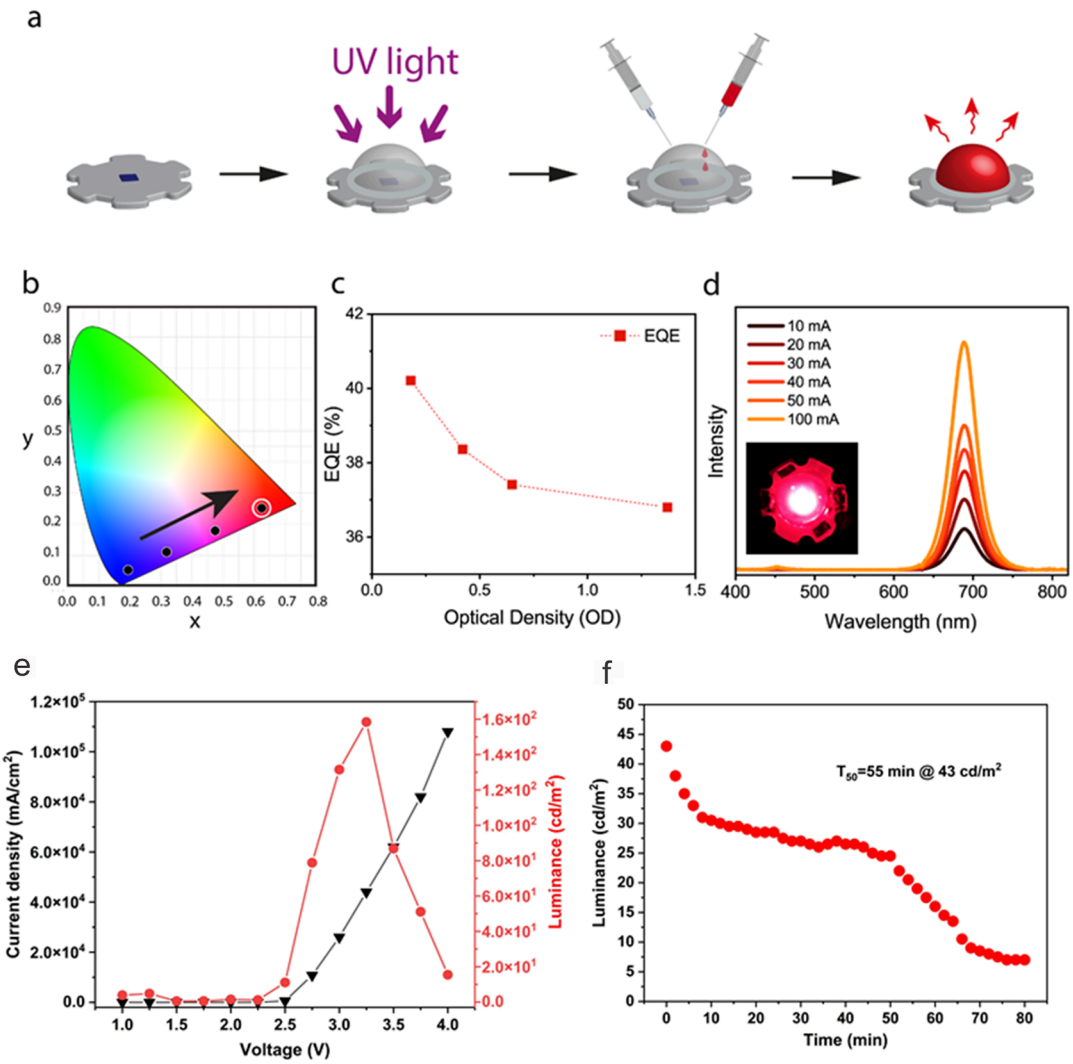


Figure 7. (a) Schematic representation of the LED fabrication process incorporating $CsPb_{1-x}Ag_xI_3$ QDs (x = 0.025 AgCl + 0.025 AgI) in a liquid form. (b) Chromaticity diagram illustrating the (x, y) color coordinates. (c) EQE of the PQD-LEDs measured at varying optical densities. (d) Emission spectra of the $CsPb_{0.95}Ag_{0.05}I_3$ (x = 0.025 AgCl + 0.025 AgI) QD LED at an optical density of 1.37 under different current injection levels ranging from 10 to 100 mA (inset: photograph of the illuminated $CsPb_{0.95}Ag_{0.05}I_3$ QD LED). (e) $J-V-L$ characteristics and (f) operational half-lifetime T_{50} of the $CsPb_{0.95}Ag_{0.05}I_3$ QD-based LED device.

some particles, likely due to surface relaxation, with no significant aggregation or coalescence, indicating excellent long-term morphological stability. In addition to UV stability, we also assessed the long-term performance of the optimized $CsPb_{0.95}Ag_{0.05}I_3$ QDs under ambient air storage, as shown in Figure S13. Remarkably, the QDs retained 43.5% of their initial PLQY even after 90 days, comparable to the 41.12% retention observed under continuous UV irradiation for 70 days (Figure 6a). This result highlights the robustness of the dual AgCl and AgI doping strategy not only against photoinduced degradation but also under environmental exposure, further supporting its potential for practical optoelectronic applications.

XRD patterns (Figure 6c) show that the dominant cubic α-$CsPbI_3$ phase was largely preserved even after 70 days. Minor peaks corresponding to the orthorhombic γ-phase emerged at later time points (day 63 onward), suggesting a slow and partial phase transition. Nonetheless, the persistence of the cubic structure demonstrates the effectiveness of synergistic AgCl and AgI codoping along with surface passivation by an I^-/Cl^- approach in delaying phase degradation.

3.5. LED Performance. To evaluate the practical applicability of the optimized QDs, $CsPb_{1-x}Ag_xI_3$ (x = 0.025 AgCl + 0.025 AgI) chosen for their exceptional PLQY and structural stability were integrated into prototype LED devices. A liquid-phase deposition approach was employed, wherein QDs (20 mg/mL in octane) were introduced onto blue LED chips to mitigate host material effects while preserving their PLQY in the device architecture.[53,54]

PDMS was selected as the encapsulating medium due to its high transparency, scalability, and cost-effectiveness in large-scale production.[55] Additionally, PDMS exhibited self-repairing capabilities, enabling surface recovery following PQD injection and preventing leakage by forming a stable containment layer atop the LED chip.

Following fabrication, the polymeric lens was carefully positioned over the blue LED chip and sealed along the edges with a UV-curable polymer (Figure 7a). After curing, residual air was evacuated using micro syringes, which were subsequently employed to inject QDs into the cavity formed between the LED PCB board and the hemispherical lens. Upon forward biasing of the blue LED, the embedded QDs

https://doi.org/10.1021/acsanm.5c03682
ACS Appl. Nano Mater. 2025, 8, 20902−20914

were optically excited, leading to strong photoluminescence in the red spectral region (Figure 7d, inset).

With increasing $CsPb_{0.95}Ag_{0.05}I_3$ QD optical density from 0.18 to 1.37, the corresponding chromaticity coordinates (x, y) exhibited notable shifts of 0.43 and 0.19, respectively (Figure 7b). The EQE of the fabricated PQD-LEDs was assessed as a function of PQD optical density (see Figure 7c). Importantly, the reported maximum EQE of 36.8% refers to the performance of the entire device, encompassing both the blue LED pump and the red-emitting perovskite QD conversion layer. This value therefore represents the operational efficiency of the assembled LED, not solely the intrinsic emission efficiency of the QDs, serving as a precise measure of device-level performance.

As the optical density increased, a reduction in EQE was observed due to reabsorption effects, with the red-emitting PQD-LED achieving a peak EQE of 36.8%. Spectral stability under a broad current injection range (10−100 mA) was also assessed (Figure 7d). The emission peak remained spectrally stable, with no observable red- or blueshift, confirming that the QD emission is resilient to current-induced heating and optical stress. This robustness under continuous operation highlights the device stability and suitability of the mixed-doped QDs for practical optoelectronic applications.

Current density/voltage vs luminance (J−V−L) measurements revealed that the maximum luminance of 158 cd/m^2 was achieved at 3.25 V, after which the luminance sharply declined to 15 cd/m^2 at higher voltages (Figure 7e). This decrease is attributed to thermal effects occurring at elevated operating voltages, where heating of the blue LED chip accelerates the degradation of the $CsPb_{0.95}Ag_{0.05}I_3$ QDs. Extended exposure to intense blue light and elevated temperatures cause octane to gradually evaporate through microscopic holes on the surface of lens, leading to the drying of QDs and their exposure to air, which can be potentially solved by replacing with a nonporous solid lens (e.g., glass). The combined impact of oxygen penetration through PDMS, light, and heat subsequently accelerates QD degradation, leading to significant luminance reduction at high voltage levels.[56] The interaction of the heat with QDs can be overcome by a remote phosphor approach. Additionally, the current density exhibited a proportional increase with rising voltage, reaching 108 × 10^3 mA/cm^2 at 4 V, demonstrating a linear voltage−current density relationship. Furthermore, the excessive current density serves as an additional driving force for thermal-induced degradation of the PQDs.[57] Accordingly, the current density of 44 × 10^3 mA/cm^2 measured at 3.25 V, corresponding to the maximum luminance, was identified as the threshold at which thermal degradation of PQDs initiates. The operational device stability for half-lifetime (T_{50}) is measured by about 55 min with the initial luminance setting at 43 cd/m^2 by applying a continuous 5 mA current (Figure 7f). The remarkable EQE value and the device stability highlight the suitability of the $CsPb_{0.95}Ag_{0.05}I_3$ PQDs for practical optoelectronic applications.

4. CONCLUSIONS

This study demonstrates that controlled Ag^+ doping combined with halide (Cl^- and I^-) passivation significantly enhances the structural stability and optoelectronic performance of $CsPbI_3$ QDs. Partial substitution of Pb^{2+} with smaller Ag^+ ions induces lattice contraction and stabilizes the α-phase, while surface-localized Cl^- and I^- ions efficiently passivate halide vacancies, suppressing nonradiative recombination. Among the various doping strategies explored, the mixed doping approach employing AgCl and AgI precursors (x = 0.025 AgCl + 0.025 AgI) provides optimal synergistic passivation effects, substantially elevating PLQY to over 96%. Crucially, the dual-doping strategy significantly mitigates the intrinsic instability of $CsPbI_3$, maintaining the cubic perovskite structure and preserving optical performance under prolonged ultraviolet exposure. Stability testing reveals sustained photoluminescence and structural integrity, with approximately 41% of the initial PLQY retained after 70 days, highlighting an important advancement toward overcoming the instability barrier for practical applications.

Device integration tests confirmed the practical potential of this approach, with prototype LEDs achieving EQEs of 36.8% and delivering bright and saturated red emission. The simple liquid-phase deposition and PDMS encapsulation underscore the scalability and manufacturability of the method, while $CsPb_{0.95}Ag_{0.05}I_3$ PQDs provide high luminance and remarkable EQE with stability suitable for optoelectronic applications, despite thermal-induced degradation at elevated voltages.

Overall, these findings not only validate the effectiveness of Ag^+ and halide codoping as a promising strategy for stabilizing $CsPbI_3$ perovskite QDs but also provide a robust foundation for further material design and optimization. Future work could explore extending this doping methodology to other perovskite compositions and optoelectronic device structures, ultimately accelerating the commercialization of high-performance, stable perovskite-based technologies.

■ ASSOCIATED CONTENT

Supporting Information

The Supporting Information is available free of charge at https://pubs.acs.org/doi/10.1021/acsanm.5c03682.

Data and analyses for XRD patterns, XPS spectra, HR-TEM and TEM analysis, EDS results, PLQY, lifetime, and absorbance spectra (PDF)

■ AUTHOR INFORMATION

Corresponding Author

Umut Aydemir − *Koç University Boron and Advanced Materials Application and Research Center (KUBAM), Istanbul 34450, Türkiye; Department of Chemistry, Koç University, Istanbul 34450, Türkiye; Department of Materials Science and Engineering, Northwestern University, Evanston, Illinois 60208, United States;* orcid.org/0000-0003-1164-1973; Email: uaydemir@ku.edu.tr, umut.aydemir@northwestern.edu

Authors

Pouriya Naziri − *Graduate School of Sciences and Engineering, Koç University, Istanbul 34450, Türkiye; Koç University Boron and Advanced Materials Application and Research Center (KUBAM), Istanbul 34450, Türkiye;* orcid.org/0000-0003-3090-9103

Asim Onal − *Graduate School of Biomedical Science and Engineering, Koç University, Istanbul 34450, Türkiye;* orcid.org/0000-0003-3682-6042

Paul Simon − *Max-Planck-Institut für Chemische Physik fester Stoffe, Dresden 01187, Germany;* orcid.org/0000-0003-1115-4024

Saba Sepahban Shahgoli − *Graduate School of Sciences and Engineering, Koç University, Istanbul 34450, Türkiye; Koç*

https://doi.org/10.1021/acsanm.5c03682
ACS Appl. Nano Mater. 2025, 8, 20902−20914

University Boron and Advanced Materials Application and Research Center (KUBAM), Istanbul 34450, Türkiye; orcid.org/0009-0004-0623-1931

Alp Yilmaz − *Graduate School of Sciences and Engineering, Koç University, Istanbul 34450, Türkiye*

Naeimeh Sadat Peighambardoust − *Koç University Boron and Advanced Materials Application and Research Center (KUBAM), Istanbul 34450, Türkiye*

Sedat Nizamoglu − *Department of Electrical and Electronics Engineering, Koç University, Istanbul 34450, Türkiye;* orcid.org/0000-0003-0394-5790

Complete contact information is available at: https://pubs.acs.org/10.1021/acsanm.5c03682

Notes

The authors declare no competing financial interest.

■ ACKNOWLEDGMENTS

The authors would like to express their deep gratitude to Dr. Hadi Jahangiri from the Koç University Surface Science and Technology Center (KUYTAM) for his invaluable assistance in the optical characterization processes.

■ REFERENCES

(1) Tian, J.; Xue, Q.; Yao, Q.; Li, N.; Brabec, C. J.; Yip, H.-L. Inorganic Halide Perovskite Solar Cells: Progress and Challenges. *Adv. Energy Mater.* **2020**, *10* (23), No. 2000183.

(2) Naziri, P.; Simon, P.; Onal, A.; Nizamoglu, S.; Aydemir, U.; Peighambardoust, N. S. Survey of Synergistically Doped $CsPbI_3$ Quantum Dots for LED Applications. *ACS Appl. Nano Mater.* **2024**, *7* (14), 16735−16748.

(3) Grisorio, R.; Fanizza, E.; Striccoli, M.; Altamura, D.; Giannini, C.; Allegretta, I.; Terzano, R.; Suranna, G. P. Shape Tailoring of Iodine-Based Cesium Lead Halide Perovskite Nanocrystals in Hot-Injection Methods. *ChemNanoMat* **2020**, *6* (3), 356−361.

(4) Xu, Y.; Wang, Q.; Zhang, L.; Lyu, M.; Lu, H.; Bai, T.; Liu, F.; Wang, M.; Zhu, J. Strontium-Doped $CsPbI_3$ Quantum Dots as an Interfacial Layer for Efficient Inorganic Perovskite Solar Cells. *Sol. RRL* **2021**, *5* (12), No. 2100669.

(5) Wei, H.; Ji, X.; Cao, J.; He, W.; Liu, H.; Pan, Z.; Song, X.; Sun, Q.; Li, J.; Wu, C. High-Performance $CsPbI_3$ Quantum Dot Photodetector with a Vertical Structure Based on the Frenkel−Poole Emission Effect. *ACS Nano* **2024**, *18* (39), 26643−26654.

(6) Biswas, S.; Panda, M. K.; Chatterjee, S.; Satra, J.; Sharma, S. K.; Rath, J.; Dutta, A.; Acharjee, D.; Chakraborty, S.; Ghosh, S.; Mishra, N. Synergistic Mitigation of Phase Segregation and Blinking Suppression Along with Enhanced Electrocatalytic Activity in $CsPbBrI_2$ Perovskite Nanocrystals via Ascorbic Acid Surface Treatment. *Adv. Funct. Mater.* **2025**, 2505506.

(7) Gong, W.; Li, Y.; Yang, Y.; Guo, H.; Niu, X. Enhanced Charge Transport from Pd-Doping in $CsPbBr_3$ Quantum Dots for Efficient Photoelectrocatalytic Water Splitting. *J. Mater. Chem. C* **2023**, *11* (21), 6963−6970.

(8) Peighambardoust, N. S.; Sadeghi, E.; Aydemir, U. Lead Halide Perovskite Quantum Dots for Photovoltaics and Photocatalysis: A Review. *ACS Appl. Nano Mater.* **2022**, *5* (10), 14092−14132.

(9) Lim, S.; Han, S.; Kim, D.; Min, J.; Choi, J.; Park, T. Key Factors Affecting the Stability of $CsPbI_3$ Perovskite Quantum Dot Solar Cells: A Comprehensive Review. *Adv. Mater.* **2023**, *35* (4), No. 2203430.

(10) Faheem, M. B.; Khan, B.; Feng, C.; Farooq, M. U.; Raziq, F.; Xiao, Y.; Li, Y. All-Inorganic Perovskite Solar Cells: Energetics, Key Challenges, and Strategies toward Commercialization. *ACS Energy Lett.* **2020**, *5* (1), 290−320.

(11) Yao, J.-S.; Ge, J.; Wang, K.-H.; Zhang, G.; Zhu, B.-S.; Chen, C.; Zhang, Q.; Luo, Y.; Yu, S.-H.; Yao, H.-B. Few-Nanometer-Sized α-$CsPbI_3$ Quantum Dots Enabled by Strontium Substitution and Iodide Passivation for Efficient Red-Light Emitting Diodes. *J. Am. Chem. Soc.* **2019**, *141* (5), 2069−2079.

(12) Dutt, V. G. V.; Akhil, S.; Singh, R.; Palabathuni, M.; Mishra, N. High-Quality $CsPbX_3$ (X = Cl, Br, or I) Perovskite Nanocrystals Using Ascorbic Acid Post-Treatment: Implications for Light-Emitting Applications. *ACS Appl. Nano Mater.* **2022**, *5* (5), 5972−5982.

(13) Zhao, B.; Jin, S.-F.; Huang, S.; Liu, N.; Ma, J.-Y.; Xue, D.-J.; Han, Q.; Ding, J.; Ge, Q.-Q.; Feng, Y.; Hu, J.-S. Thermodynamically Stable Orthorhombic γ-$CsPbI_3$ Thin Films for High-Performance Photovoltaics. *J. Am. Chem. Soc.* **2018**, *140* (37), 11716−11725.

(14) Chatterjee, S.; Biswas, S.; Sourav, S.; Rath, J.; Akhil, S.; Mishra, N. Strategies To Achieve Long-Term Stability in Lead Halide Perovskite Nanocrystals and Its Optoelectronic Applications. *J. Phys. Chem. Lett.* **2024**, *15* (40), 10118−10137.

(15) Straus, D. B.; Guo, S.; Abeykoon, A. M. M.; Cava, R. J. Understanding the Instability of the Halide Perovskite $CsPbI_3$ through Temperature-Dependent Structural Analysis. *Adv. Mater.* **2020**, *32* (32), 2001069.

(16) Khan, J.; Ullah, I.; Yuan, J. $CsPbI_3$ Perovskite Quantum Dot Solar Cells: Opportunities, Progress and Challenges. *Mater. Adv.* **2022**, *3* (4), 1931−1952.

(17) Bi, C.; Sun, X.; Huang, X.; Wang, S.; Yuan, J.; Wang, J. X.; Pullerits, T.; Tian, J. Stable $CsPb_{1-X}Zn_xI_3$ Colloidal Quantum Dots with Ultralow Density of Trap States for High-Performance Solar Cells. *Chem. Mater.* **2020**, *32* (14), 6105−6113.

(18) Liu, C.; Hu, M.; Zhou, X.; Wu, J.; Zhang, L.; Kong, W.; Li, X.; Zhao, X.; Dai, S.; Xu, B.; Cheng, C. Efficiency and Stability Enhancement of Perovskite Solar Cells by Introducing $CsPbI_3$ Quantum Dots as an Interface Engineering Layer. *NPG Asia Mater.* **2018**, *10* (6), 552−561.

(19) Xiao, S.; Mei, X.; Zhang, X. Surface Matrix Regulation of Perovskite Quantum Dots for Efficient Solar Cells. *Energy Environ. Sci.* **2024**, *17* (16), 5756−5794.

(20) Kim, D.; Yun, T.; An, S.; Lee, C.-L. How to Improve the Structural Stabilities of Halide Perovskite Quantum Dots: Review of Various Strategies to Enhance the Structural Stabilities of Halide Perovskite Quantum Dots. *Nano Converg.* **2024**, *11* (1), 4.

(21) Yoon, H. C.; Lee, S.; Song, J. K.; Yang, H.; Do, Y. R. Efficient and Stable $CsPbBr_3$ Quantum-Dot Powders Passivated and Encapsulated with a Mixed Silicon Nitride and Silicon Oxide Inorganic Polymer Matrix. *ACS Appl. Mater. Interfaces* **2018**, *10* (14), 11756−11767.

(22) Chen, Y.; Liu, Y.; Hong, M. Cation-Doping Matters in Caesium Lead Halide Perovskite Nanocrystals: From Physicochemical Fundamentals to Optoelectronic Applications. *Nanoscale* **2020**, *12* (23), 12228−12248.

(23) Huang, X.; Hu, J.; Bi, C.; Yuan, J.; Lu, Y.; Sui, M.; Tian, J. B-Site Doping of $CsPbI_3$ Quantum Dot to Stabilize the Cubic Structure for High-Efficiency Solar Cells. *Chem. Eng. J.* **2021**, *421*, No. 127822.

(24) Ma, X.; Yang, L.; Lei, K.; Zheng, S.; Chen, C.; Song, H. Doping in Inorganic Perovskite for Photovoltaic Application. *Nano Energy* **2020**, *78*, No. 105354.

(25) Bian, L.; Cao, F.; Li, L. Performance Improvement of Lead-Based Halide Perovskites through B-Site Ion-Doping Strategies. *Small* **2023**, *19* (36), No. 2302700.

(26) Zhang, L.; Zhou, H.; Chen, Y.; Zheng, Z.; Huang, L.; Wang, C.; Dong, K.; Hu, Z.; Ke, W.; Fang, G. Spontaneous Crystallization of Strongly Confined $CsSn_xPb_{1-X}I_3$ Perovskite Colloidal Quantum Dots at Room Temperature. *Nat. Commun.* **2024**, *15* (1), 1609.

(27) Liu, M.; Jiang, N.; Wang, Z.; Zheng, Y.; Hong, J.; Du, S.; Chen, D. Mn^{2+}-Doped $CsPbI_3$ Nanocrystals for Perovskite Light-Emitting Diodes with High Luminance and Improved Device Stability. *Adv. Photonics Res.* **2021**, *2* (11), 2100137.

(28) Roy, B.; Mahato, S.; Bose, S.; Ghorai, A.; Srivastava, S. K.; Das, N. C.; Ray, S. K. Cu-Doping Induced Phase Transformation in $CsPbI_3$ Nanocrystals with Enhanced Structural Stability and Photoluminescence Quantum Yield. *Chem. Mater.* **2023**, *35* (4), 1601−1609.

(29) Lu, M.; Zhang, X.; Zhang, Y.; Guo, J.; Shen, X.; Yu, W. W.; Rogach, A. L. Simultaneous Strontium Doping and Chlorine Surface

Passivation Improve Luminescence Intensity and Stability of $CsPbI_3$ Nanocrystals Enabling Efficient Light-Emitting Devices. *Adv. Mater.* **2018**, *30* (50), 1804691.
(30) Wang, J.; Zhang, C.; Li, S.; Guo, Q.; Bai, Y.; Jia, G. Simultaneous Enhancement of the Luminescence Intensity and Stability of Deep-Red $CsPbI_3$ Perovskite Quantum Dots Achieved by a Doping Strategy. *Langmuir* **2023**, *39* (32), 11317−11328.
(31) Shi, J.; Li, F.; Yuan, J.; Ling, X.; Zhou, S.; Qian, Y.; Ma, W. Efficient and Stable $CsPbI_3$ Perovskite Quantum Dots Enabled by in Situ Ytterbium Doping for Photovoltaic Applications. *J. Mater. Chem. A* **2019**, *7* (36), 20936−20944.
(32) Shu, B.; Chang, Y.; Zhang, J.; Cheng, X.; Yu, D. Synthesis and Photoluminescence Kinetics of Ce^{3+}-Doped $CsPbI_3$ QDs with near-Unity PLQY. *Nano Res.* **2021**, *14* (10), 3352−3357.
(33) Xia, W.; Ren, Z.; Zheng, Z.; Luo, C.; Li, J.; Ma, W.; Zhou, X.; Chen, Y. Highly Stable Lanthanide-Doped $CsPbI_3$ Perovskite Nanocrystals with near-Unity Quantum Yield for Efficient Red Light-Emitting Diodes. *Nanoscale* **2023**, *15* (3), 1109−1118.
(34) Li, X.; Wang, K.; Lgbari, F.; Dong, C.; Yang, W.; Ma, C.; Ma, H.; Wang, Z.-K.; Liao, L.-S. Indium Doped $CsPbI_3$ Films for Inorganic Perovskite Solar Cells with Efficiency Exceeding 17%. *Nano Res.* **2020**, *13* (8), 2203−2208.
(35) Steele, J. A.; Prakasam, V.; Huang, H.; Solano, E.; Chernyshov, D.; Hofkens, J.; Roeffaers, M. B. J. Trojans That Flip the Black Phase: Impurity-Driven Stabilization and Spontaneous Strain Suppression in γ-$CsPbI_3$ Perovskite. *J. Am. Chem. Soc.* **2021**, *143* (28), 10500−10508.
(36) Meggiolaro, D.; Motti, S. G.; Mosconi, E.; Barker, A. J.; Ball, J.; Andrea Riccardo Perini, C.; Deschler, F.; Petrozza, A.; De Angelis, F. Iodine Chemistry Determines the Defect Tolerance of Lead-Halide Perovskites. *Energy Environ. Sci.* **2018**, *11* (3), 702−713.
(37) Zhang, L.; Kang, C.; Zhang, G.; Pan, Z.; Huang, Z.; Xu, S.; Rao, H.; Liu, H.; Wu, S.; Wu, X.; Li, X.; Zhu, Z.; Zhong, X.; Jen, A. K.-Y. All-Inorganic $CsPbI_3$ Quantum Dot Solar Cells with Efficiency over 16% by Defect Control. *Adv. Funct. Mater.* **2021**, *31* (4), 2005930.
(38) Li, J.; Xu, L.; Wang, T.; Song, J.; Chen, J.; Xue, J.; Dong, Y.; Cai, B.; Shan, Q.; Han, B.; Zeng, H. 50-Fold EQE Improvement up to 6.27% of Solution-Processed All-Inorganic Perovskite $CsPbBr_3$ QLEDs via Surface Ligand Density Control. *Adv. Mater.* **2017**, *29* (5), 1603885.
(39) Guo, J.; Lu, M.; Zhang, X.; Sun, S.; Han, C.; Zhang, Y.; Yang, X.; Kershaw, S. V.; Zheng, W.; Rogach, A. L. Highly Stable and Efficient Light-Emitting Diodes Based on Orthorhombic γ-$CsPbI_3$ Nanocrystals. *ACS Nano* **2023**, *17* (10), 9290−9301.
(40) Lu, M.; Guo, J.; Lu, P.; Zhang, L.; Zhang, Y.; Dai, Q.; Hu, Y.; Colvin, V. L.; Yu, W. W. Ammonium Thiocyanate-Passivated $CsPbI_3$ Perovskite Nanocrystals for Efficient Red Light-Emitting Diodes. *J. Phys. Chem. C* **2019**, *123* (37), 22787−22792.
(41) Yang, J.-N.; Song, Y.; Yao, J.-S.; Wang, K.-H.; Wang, J.-J.; Zhu, B.-S.; Yao, M.-M.; Rahman, S. U.; Lan, Y.-F.; Fan, F.-J.; Yao, H.-B. Potassium Bromide Surface Passivation on $CsPbI_{3-X}Br_x$ Nanocrystals for Efficient and Stable Pure Red Perovskite Light-Emitting Diodes. *J. Am. Chem. Soc.* **2020**, *142* (6), 2956−2967.
(42) Pan, J.; Shang, Y.; Yin, J.; De Bastiani, M.; Peng, W.; Dursun, I.; Sinatra, L.; El-Zohry, A. M.; Hedhili, M. N.; Emwas, A.-H.; Mohammed, O. F.; Ning, Z.; Bakr, O. M. Bidentate Ligand-Passivated $CsPbI_3$ Perovskite Nanocrystals for Stable Near-Unity Photoluminescence Quantum Yield and Efficient Red Light-Emitting Diodes. *J. Am. Chem. Soc.* **2018**, *140* (2), 562−565.
(43) Lu, M.; Guo, J.; Sun, S.; Lu, P.; Wu, J.; Wang, Y.; Kershaw, S. V.; Yu, W. W.; Rogach, A. L.; Zhang, Y. Bright $CsPbI_3$ Perovskite Quantum Dot Light-Emitting Diodes with Top-Emitting Structure and a Low Efficiency Roll-Off Realized by Applying Zirconium Acetylacetonate Surface Modification. *Nano Lett.* **2020**, *20* (4), 2829−2836.
(44) Chen, J.; Su, Y.; Shen, Y.; Liu, X.; Xiang, H.; Duan, L.; Zeng, H. Synergistic Passivation of Alkali Halides Enables Highly Efficient Perovskite QLEDs. *J. Mater. Chem. C* **2024**, *12* (5), 1870−1876.
(45) Shannon, R. D. Revised Effective Ionic Radii and Systematic Studies of Interatomic Distances in Halides and Chalcogenides. *Acta Crystallogr., Sect. A* **1976**, *32* (5), 751−767.
(46) Zhu, H.; Hao, C.; Li, X.; Qi, Y.; Zhu, X.; Miao, Y.; Liu, R.; Ding, J. Long-Term Stability in α-$CsPbI_3$ Quantum Dots via a Nonvacuum Ag^+ Doping Strategy. *J. Phys. Chem. C* **2023**, *127* (37), 18727−18735.
(47) Lin, Y.; Shao, Y.; Dai, J.; Li, T.; Liu, Y.; Dai, X.; Xiao, X.; Deng, Y.; Gruverman, A.; Zeng, X. C.; Huang, J. Metallic Surface Doping of Metal Halide Perovskites. *Nat. Commun.* **2021**, *12* (1), 7.
(48) Woo, J. Y.; Kim, Y.; Bae, J.; Kim, T. G.; Kim, J. W.; Lee, D. C.; Jeong, S. Highly Stable Cesium Lead Halide Perovskite Nanocrystals through in Situ Lead Halide Inorganic Passivation. *Chem. Mater.* **2017**, *29* (17), 7088−7092.
(49) Akkerman, Q. A.; Meggiolaro, D.; Dang, Z.; De Angelis, F.; Manna, L. Fluorescent Alloy $CsPb_xMn_{1-X}I_3$ Perovskite Nanocrystals with High Structural and Optical Stability. *ACS Energy Lett.* **2017**, *2* (9), 2183−2186.
(50) Li, M.; Xu, J.; Song, Y.; Chen, F. Enhance Luminescence or Change Morphology: Effect of the Doping Method on Cu^{2+}-Doped $CsPbBr_3$ Perovskite Nanocrystals. *CrystEngComm* **2022**, *24* (45), 7962−7970.
(51) Chu, A.; Luo, J.; Zhang, D.; Xie, Y.; Li, S.; He, J.; Li, M.; Jiang, J.; Wu, J.; Cai, M.; Zhuang, X. Lattice and Bandgap Modulation in Metal Halide Perovskites by B-Site Ions Substitution. *Adv. Opt. Mater.* **2025**, 2403202.
(52) Li, F.; Liu, Y.; Wang, H.; Zhan, Q.; Liu, Q.; Xia, Z. Postsynthetic Surface Trap Removal of $CsPbX_3$ (X = Cl, Br, or I) Quantum Dots via a ZnX_2/Hexane Solution toward an Enhanced Luminescence Quantum Yield. *Chem. Mater.* **2018**, *30* (23), 8546−8554.
(53) Onal, A.; Eren, G. O.; Sadeghi, S.; Melikov, R.; Han, M.; Karatum, O.; Ozer, M. S.; Bahmani Jalali, H.; Dogru-Yuksel, I. B.; Yilgor, I.; Metin, Ö.; Nizamoglu, S. High-Performance White Light-Emitting Diodes over 150 Lm/W Using Near-Unity-Emitting Quantum Dots in a Liquid Matrix. *ACS Photonics* **2022**, *9* (4), 1304−1314.
(54) Onal, A.; Eren, G. O.; Melikov, R.; Kaya, L.; Nizamoglu, S. Quantum Dot Enabled Efficient White LEDs for Wide Color Gamut Displays. *Adv. Mater. Technol.* **2023**, *8* (9), 2201799.
(55) Sadeghi, S.; Ganesh Kumar, B.; Melikov, R.; Mohammadi Aria, M.; Bahmani Jalali, H.; Nizamoglu, S. Quantum Dot White LEDs with High Luminous Efficiency. *Optica* **2018**, *5* (7), 793−802.
(56) Akbulatov, A. F.; Frolova, L. A.; Dremova, N. N.; Zhidkov, I.; Martynenko, V. M.; Tsarev, S. A.; Luchkin, S. Y.; Kurmaev, E. Z.; Aldoshin, S. M.; Stevenson, K. J.; Troshin, P. A. Light or Heat: What Is Killing Lead Halide Perovskites under Solar Cell Operation Conditions? *J. Phys. Chem. Lett.* **2020**, *11* (1), 333−339.
(57) Zou, C.; Liu, Y.; Ginger, D. S.; Lin, L. Y. Suppressing Efficiency Roll-Off at High Current Densities for Ultra-Bright Green Perovskite Light-Emitting Diodes. *ACS Nano* **2020**, *14* (5), 6076−6086.

https://doi.org/10.1021/acsanm.5c03682
ACS Appl. Nano Mater. 2025, 8, 20902−20914